Fractionalized excitations probed by ultrasound

A. Hauspurg,[1,2] S. Zherlitsyn,[1] T. Helm,[1] V. Felea,[1] J. Wosnitza,[1,2] V. Tsurkan,[3,4] K.-Y. Choi,[5] S.-H. Do,[6] Mengxing Ye,[7,8] Wolfram Brenig,[9] and Natalia B. Perkins[10,11]

[1]*Hochfeld-Magnetlabor Dresden (HLD-EMFL) and Würzburg-Dresden Cluster of Excellence ct.qmat, Helmholtz-Zentrum Dresden-Rossendorf (HZDR), 01328 Dresden, Germany*

[2]*Institut für Festkörper- und Materialphysik, Technische Universität Dresden, 01062 Dresden, Germany*

[3]*Experimental Physics V, Center for Electronic Correlations and Magnetism, University of Augsburg, 86135 Augsburg, Germany*

[4]*Institute of Applied Physics, Moldova State University, MD 2028, Chisinau, Republic of Moldova*

[5]*Department of Physics, Sungkyunkwan University, Suwon 16419, Republic of Korea*

[6]*Materials Science and Technology Division, Oak Ridge National Laboratory, Oak Ridge, Tennessee 37831, USA*

[7]*Kavli Institute for Theoretical Physics, University of California, Santa Barbara, California 93106, USA*

[8]*Department of Physics and Astronomy, University of Utah, Salt Lake City, Utah 84112, USA*

[9]*Institute for Theoretical Physics, Technical University Braunschweig, 38106 Braunschweig, Germany*

[10]*School of Physics and Astronomy, University of Minnesota, Minneapolis, Minnesota 55455, USA*

[11]*Technical University of Munich, Germany, Institute for Advanced Study, 85748 Garching, Germany*

(Received 9 March 2023; accepted 28 March 2024; published 18 April 2024)

In this work, we study magnetoelastic interactions by means of ultrasound experiments in α-$RuCl_3$—a prototypical material for the Kitaev spin model on the honeycomb lattice, with a possible spin-liquid state featuring Majorana fermions and $\mathbb{Z}_2$-flux excitations. We present results of the temperature and in-plane magnetic-field dependence of the sound velocity and sound attenuation for several longitudinal and transverse phonon modes propagating along high-symmetry crystallographic directions. A comprehensive data analysis above the magnetically ordered state provides strong evidence of phonon scattering by Majorana fermions. This scattering depends sensitively on the value of the phonon velocities relative to the characteristic velocity of the low-energy fermionic excitations describing the spin dynamics of the underlying Kitaev magnet. Moreover, our data displays a distinct reduction of anisotropy of the sound attenuation, consistent with the presence of thermally excited $\mathbb{Z}_2$ visons. We demonstrate the potential of phonon dynamics as a promising probe for uncovering fractionalized excitations in α-$RuCl_3$ and provide new insights into the H-T phase diagram of this material.

DOI: 10.1103/PhysRevB.109.144415

I. INTRODUCTION

A hallmark of a quantum spin liquid (QSL) is spin fractionalization. In the exactly solvable Kitaev model spin excitations are fractionalized into two types of quasiparticles: itinerant spinon-like excitations, which are described by Majorana fermions, and localized gapped $\mathbb{Z}_2$ fluxes [1,2]. Recent theoretical studies have shown that the characteristic signatures of such a spin fractionalization can be observed experimentally using various dynamical probes [3–14]. Phonon dynamics is another indirect but promising probe to explore QSL physics in real materials [15–21], since spin-lattice coupling is inevitable and often rather strong in real materials with large spin-orbit coupling.

The spin-orbit-coupled Mott insulator α-$RuCl_3$ is among the most extensively studied materials predicted to host Kitaev interactions and to be in proximity to the Kitaev QSL state [14,22–26]. Despite the presence of non-Kitaev interactions in this material leading to a zigzag antiferromagnetic order below $T_N = 7.1$ K [27–31], much effort has been devoted to searching for traces of fractionalization in the spin dynamics of α-$RuCl_3$ [23,32–39]. However, how close this material is to the Kitaev QSL remains an open question both at zero and applied magnetic field [31,40].

It was realized that the magnetoelastic coupling plays an important role in the interpretation of thermal-Hall transport measurements [37,41,42]. Therefore, the research focus has shifted further towards this aspect [43–46] producing insights into the spin-phonon interactions in this material [37,47–51]. Mobile Majorana fermions and thermally induced static $\mathbb{Z}_2$ gauge fluxes lead to a continuum of scattering processes, which strongly affect the phonon dynamics and dissipation [17–19]. In particular, low-temperature sound attenuation due to phonon scattering from fermionic particle-hole excitations is predicted to be linear in temperature [17,18], and to show rotational symmetry breaking to C_{6v} symmetry [18,19]. Furthermore, time-reversal symmetry breaking by a magnetic field results in a Hall viscosity, which mixes the longitudinal and transverse phonon modes, and allows for phonon Berry curvatures [18].

In this work, we report on a study of the spin dynamics in α-$RuCl_3$ by means of ultrasound, examining the theoretical predictions related to the sound velocity and attenuation in the Kitaev material [17,18]. From the temperature and in-plane magnetic-field dependence of the attenuation of sound waves, we conclude that phonons are scattered off fractionalized excitations associated with the underlying Kitaev magnet. The difference in the sound attenuation of the longitudinal and

transverse phonon modes can be understood by the value of phonon velocities with respect to the characteristic velocity of the low-energy fermionic excitations. Remarkably, due to a significant difference in the velocities of the longitudinal and transverse phonon modes being larger and smaller than the velocity of dispersing Majorana fermions, respectively, the phonon dynamics in α-$RuCl_3$ exhibits two different regimes of attenuation: (1) a phonon scatters an occupied fermion state to a higher-energy state [ph channel, Fig. 2(d)], and (2) a phonon decays into two fermions, both with positive energy [pp channel, Fig. 2(e)]. In the former case, the sound attenuation increases linearly with T. In the latter case, it is almost temperature independent, only slightly decreasing with T for temperatures above 30–40 K. Furthermore, thanks to the high sensitivity of ultrasound to various phase transitions [52,53], we performed a detailed investigation of the H-T phase diagram of α-$RuCl_3$ for an in-plane magnetic field applied perpendicular to the Ru-Ru bonds.

II. METHODS

We grew high-quality single crystals by vacuum sublimation [31,54]. Our samples show a single phase transition at 7.1 K and no signatures of an additional phase transition at 14 K, which could be caused by stacking faults. While the trigonal $P3_112$ space group of α-$RuCl_3$ has been reported at room temperature [55], the low-temperature symmetry of this compound is still under debate [46,56]. In our investigation, we oriented the samples using Laue x-ray backscattering diffraction technique. Analysis of the anisotropic suppression of magnetic order with in-plane magnetic fields confirms the sample orientation. There are two distinguished crystallographic directions in the honeycomb plane: the **a** axis perpendicular to the Ru-Ru bonds and the **b** axis parallel to the Ru-Ru bonds [see inset in Fig. 3(c)]. The typical sample length in the honeycomb plane is 2.0 mm along the **a** direction and 1.63 mm along the **b** direction, with a characteristic size of 1 mm normal to the plane (**c** direction).

We performed bulk ultrasound measurements using a pulse-echo method with a phase-sensitive detection technique [52,57], the details of which are outlined in the Appendix. To generate and detect ultrasonic signals in the frequency range 20–120 MHz, we bonded ultrasound transducers ($LiNbO_3$, 36° Y cut for longitudinal and 41° X cut for transverse-acoustic modes) with Thiokol 32 to the two parallel sample surfaces prepared by a focused ion beam (FIB). The transducers were adapted in size and covered the prepared surfaces of the sample. Typically, several ultrasound echoes due to multiple propagations and reflections in the sample are observed in our experiments. We used a calibrated RuO_2 resistor in a ^{3}He cryostat and a Cernox sensor in a variable temperature insert (VTI) for thermometry.

Our results for the sound velocity of the longitudinal acoustic modes, corresponding to the elastic stiffness constants c_{11} and c_{33}, and of the transverse acoustic modes $(c_{11} - c_{12})/2$, and c_{44}, in the crystal assuming hexagonal symmetry at zero and finite magnetic fields are summarized in Fig. 1. The related geometries, as well as the absolute values of the ultrasound frequency f, sound velocity v_s, and wave numbers q are listed in Table I. For each of the acoustic modes, the general relationship, $c_{ij} = \rho v_s^2$, between the elastic constants, sound velocities, and mass density is satisfied. Note that as the symmetry of α-$RuCl_3$ might be lower than hexagonal (both $C2/m$ or $P3_112$ were previously reported in the literature [23,27,58]), the sound velocities of acoustic modes along the **a** and **b** axes are different.

TABLE I. Sound velocities and wave numbers for various acoustic modes and experimental settings. Here, f is the frequency, **q** the wave vector, **u** the polarization of the acoustic wave, v_s the sound velocity measured at 0.3 K at zero field, and q the corresponding wave number. Sound velocities v_s of both longitudinal c_{11} and transverse $(c_{11} - c_{12})/2$ modes agree well with results from the x-ray experiments from Li *et al.* [48,62] and Lebert *et al.* [56].

Mode	Geometry	f [MHz]	v_s [m/s]	$q = 2\pi f/v$ [μm^{-1}]
c_{33}	**q** ∥ **c**; **u** ∥ **c**	106	2900 ± 100	0.23
c_{44}	**q** ∥ **b**; **u** ∥ **c**	27	1350 ± 50	0.126
	Voigt			
c_{11}	**q** ∥ **b**; **u** ∥ **b**	40	3000 ± 200	0.084
$(c_{11} - c_{12})/2$	**q** ∥ **b**; **u** ∥ **a**	28	2400 ± 100	0.073
	Faraday			
c_{11}	**q** ∥ **a**; **u** ∥ **a**	22	3300 ± 200	0.042
$(c_{11} - c_{12})/2$	**q** ∥ **a**; **u** ∥ **b**	26	2200 ± 100	0.057

In addition to the velocity, we characterize the dissipation of the propagation of the acoustic modes by means of a sound-attenuation coefficient α. Because the signal amplitude $A'(T_0, H_0)$ (measured at the initial field H_0 and temperature T_0) depends on the experimental settings, only the change of the sound attenuation is obtained from our experiments. We define this as $\Delta\alpha(T, H) = \alpha(T, H) - \alpha(T_0, H_0) = -20 \log_{10}[A'(T, H)/A'(T_0, H_0)]/L$, where A' is the signal amplitude and L is the effective sample length (see Appendix).

III. RESULTS

A. Sound velocity and attenuation

Next, we present the main result of this paper—the experimental observation of a rich temperature and in-plane magnetic-field dependence of the sound attenuation beyond the magnetically ordered state in α-$RuCl_3$.

Figure 1 shows the temperature dependence of the relative sound velocity, $\Delta v/v$, and the change in the sound attenuation, $\Delta\alpha(T)$ in different acoustic-mode geometries; Figs. 1(a)–1(c) and 1(d)–1(f) correspond to zero field and a field of $\mu_0 H_{\mathbf{a}} = 8$ T, respectively. To begin with, this figure clearly establishes the presence of strong magnetoelastic coupling for sound propagation in α-$RuCl_3$. At zero field, shown in Figs. 1(a)–1(c), the acoustic modes exhibit pronounced anomalies at the magnetic ordering temperature T_N, which are fully consistent with the critical softening due to a second-order magnetic phase transition [59], displaying a sharp dip in $\Delta v/v(T)$ (blue lines) and a peak in $\Delta\alpha(T)$ (black lines). The inset in Fig. 1(a) shows a thermal hysteresis of the c_{33} mode at the first-order structural phase transition, presumably, from the high-temperature monoclinic to a low-temperature rhombohedral structure [60,61]. For an external

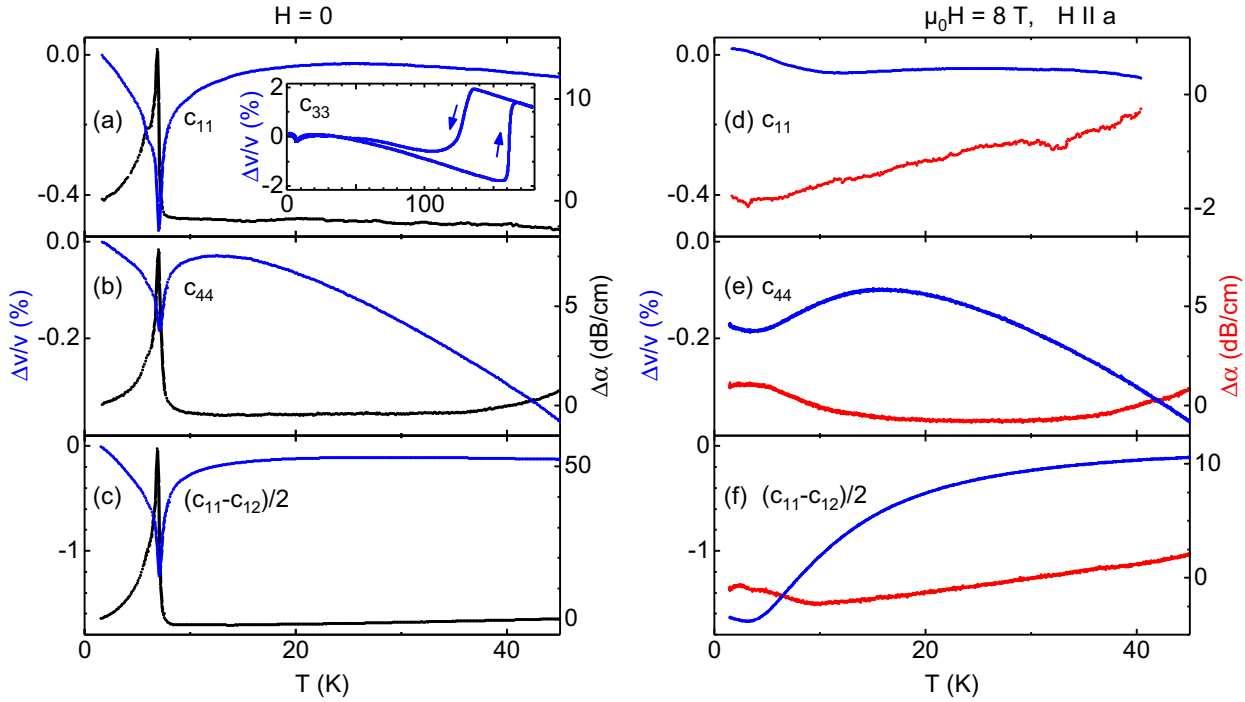

FIG. 1. Temperature dependence of the relative sound velocity (blue, left scales) and sound attenuation (black and red, right scales) of selected acoustic modes in (a)–(c) zero and in (d)–(f) magnetic field along the **a** direction with $\mu_0 H = 8$ T. The modes shown are (a), (d) c_{11}, (b), (e) c_{44}, and (c), (f) $(c_{11} - c_{12})/2$ with $\mathbf{q} \parallel \mathbf{b}$. Geometries and measurement frequencies are given in Table I. The inset in panel (a) shows the sound velocity change for the c_{33} acoustic mode up to 180 K ($f = 60$ MHz). Here, up and down sweeps are marked by arrows. Note the different attenuation scales for the data obtained in (a)–(c) zero field and (d)–(f) at $\mu_0 H = 8$ T.

magnetic field of $\mu_0 H_{\mathbf{a}} = 8$ T, the sharp anomalies both in $\Delta v/v(T)$ (blue lines) and in $\Delta\alpha(T)$ (red lines) are absent [see Figs. 1(d)–1(e)]. This is consistent with the complete suppression of long-range magnetic zigzag ordering. However, some weak minima (maxima) can still be observed in $\Delta v/v(T)$ [$\Delta\alpha(T)$] around 3–4 K, most notably for the transverse $(c_{11} - c_{12})/2$ mode [Fig. 1(f)]. These are indications for some remaining short-range magnetic fluctuations.

In Fig. 2(a), we summarize the temperature dependence of the sound-attenuation change of the longitudinal, c_{11}, and transverse, $(c_{11} - c_{12})/2$ and c_{44}, acoustic modes propagating along two high-symmetry directions, $\mathbf{q} \parallel \mathbf{a}$ and $\mathbf{q} \parallel \mathbf{b}$, in zero and in a finite magnetic field $\mathbf{H}||\mathbf{a}$. In the following, we focus on three relevant aspects. First, for a given propagation direction and magnetic field, $\Delta\alpha(T)$ varies differently with T for different modes. Second, for a fixed magnetic field, $\Delta\alpha(T)$ is different for the same mode propagating along the **a** and **b** directions, i.e., the sound attenuation is anisotropic. Third, every acoustic mode with in-plane strain exhibits different zero- and finite-field attenuation "slopes" versus temperature.

Zero-field behavior of sound attenuation. At zero magnetic field, $\Delta\alpha(T)$ shows markedly different temperature dependencies for the in-plane longitudinal, c_{11}, and the transverse, $(c_{11} - c_{12})/2$, acoustic modes in the temperature range of 10–45 K. The c_{11} mode shows an almost-temperature-independent sound attenuation, with an overall weak downturn of $\Delta\alpha(T)$, which may slightly increase above 20 K . In contrast, we observe a clear linear temperature dependence of $\Delta\alpha(T)$ for the transverse modes $(c_{11} - c_{12})/2$. To show this more clearly, we display enlarged plots of these two modes for $\mathbf{q} \parallel \mathbf{b}$ in Figs. 2(b) and 2(c), respectively. It is also remarkable that $\Delta\alpha(T)$ not only shows a very different temperature dependence for the longitudinal, c_{11}, and the transverse, $(c_{11} - c_{12})/2$, acoustic modes for the same propagation vector, but it is also quite different with respect to the same acoustic mode propagating with $\mathbf{q} \parallel \mathbf{a}$ or $\mathbf{q} \parallel \mathbf{b}$ (see Fig. 2). For example, the slope for the transverse mode, $(c_{11} - c_{12})/2$, propagating along $\mathbf{q} \parallel \mathbf{a}$ is significantly larger than that propagating along $\mathbf{q} \parallel \mathbf{b}$, clearly indicating the spatial anisotropy in the attenuation.

We rationalize these findings based on the fermionic excitations of the pure Kitaev model. In our consideration, let us first neglect thermal flux excitations and return to them later. The Fermi velocity, which is determined by the slope of the Dirac cones, can be estimated via the Kitaev coupling, $J \simeq 81$ K (7 meV), in α-$RuCl_3$ to be $v_F \simeq 2746$ m/s (18 meV Å). This is consistent with previous estimates in Ref. [62]. Previous theoretical studies [17–19] have shown that, when $v_s < v_F$, the primary contribution to the sound attenuation stems from microscopic processes, in which a phonon scatters a positive-energy fermion to a higher-energy fermion state—dubbed ph channel, schematically shown in Fig. 2(d). When $v_s > v_F$, the kinematic constraints can only be satisfied in microscopic processes where a phonon decays into two fermions, both with positive energy—dubbed pp channel in Fig. 2(e). The sound attenuation depends on

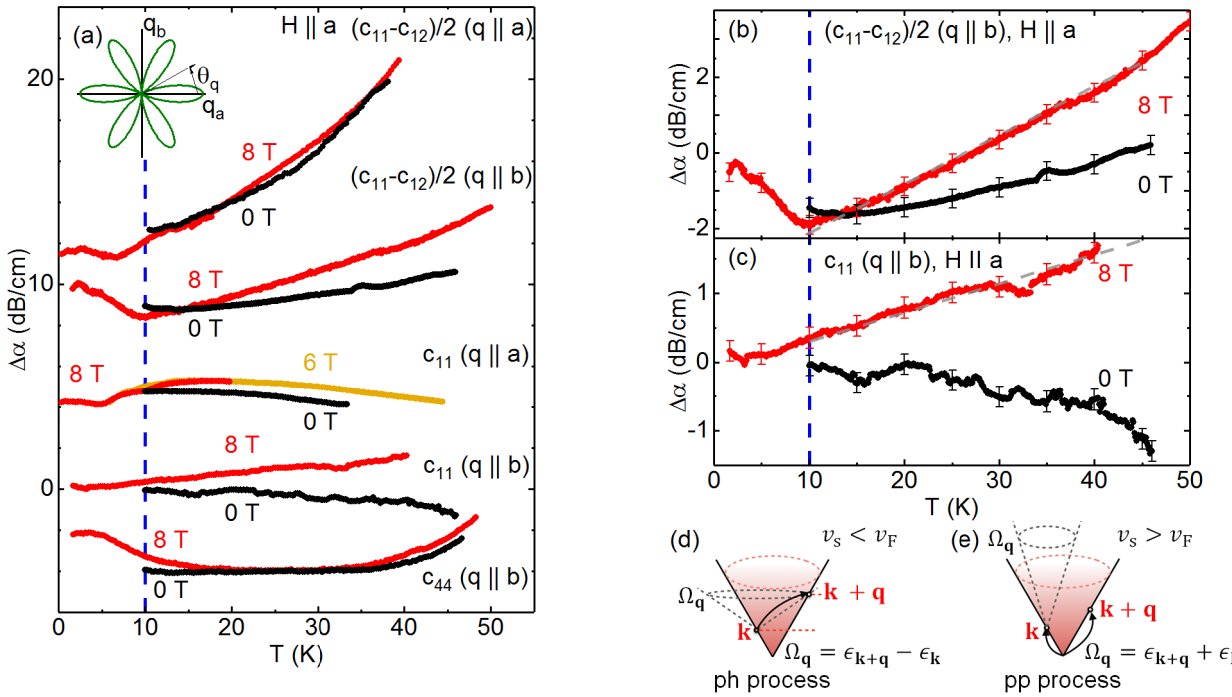

FIG. 2. (a) Change of the sound attenuation versus temperature in α-$RuCl_3$ beyond the magnetically ordered state. We show results for the longitudinal c_{11} and transverse $(c_{11} - c_{12})/2$ acoustic modes for two high-symmetry in-plane propagation directions, $\mathbf{q} \parallel \mathbf{a}$ and $\mathbf{q} \parallel \mathbf{b}$, in zero (black) and magnetic field applied along $\mathbf{a}$ (red, orange). Results for the transverse c_{44} acoustic mode ($\mathbf{q} \parallel \mathbf{b}$, $\mathbf{u} \parallel \mathbf{c}$) are also shown. The zero-field data were removed close to and below T_N (below the vertical dashed blue line) to mask the dominant attenuation anomaly [shown in Figs. 1(a)–1(c)] at the ordering temperature T_N. Panels (b) and (c) show the data from panel (a) for the acoustic mode $(c_{11} - c_{12})/2$ and c_{11}, respectively, on an enlarged scale. Measurement frequencies were in the range 20–40 MHz . Note that, for different experimental geometries (different acoustic modes and different propagation directions) the related attenuation is arbitrarily shifted for clarity. The zero- and in-field curves belonging to the same acoustic mode for a chosen propagation direction [and with the same $A'(T_0, H_0)$ defined in Sec. II] are not shifted with respect to each other. The straight dashed gray lines are guides to the eye. Panels (d) and (e) illustrate different scattering channels near the bottom of the Dirac cone with acoustic-phonon velocities $v_s < v_F$ and $v_s > v_F$, respectively. See text for details.

temperature in distinct manners for phonon decaying in the ph and pp channels. We discuss this in detail below and compare with our data.

Apparently, from Table I, the sound velocities v_s^{Ta} and v_s^{Tb} of the transverse mode $(c_{11} - c_{12})/2$ for $\mathbf{q} \parallel \mathbf{a}$ and $\mathbf{q} \parallel \mathbf{b}$, respectively, are both smaller than v_F. In this situation, the ph channel dominates. Power counting for the density of states in the vicinity of the Dirac points leads to $\Delta\alpha(T) \propto T$ when $v_s q \ll T \ll J$, i.e., linearity in temperature [17–19]. This prediction is consistent with the experimental data presented in Figs. 2(a) and 2(b).

Regarding the anisotropy of the attenuation, it was shown in Ref. [18] that the dominant contribution is due to the E_2 irreducible representation of the C_{6v} point group. For the transverse mode, this results in an angular dependence of $(1 + \cos 6\theta_q)$ [see inset in Fig. 2(a)]. This leads to a maximum attenuation of the transverse mode for $\mathbf{q} \parallel \mathbf{a}$ and none for $\mathbf{q} \parallel \mathbf{b}$. In addition to the E_2 channel, however, contributions from a subdominant A_1 channel are also present, generating an angular-independent contribution to $\Delta\alpha(T)$. This is consistent with the observed angular variation of the slope of the $(c_{11} - c_{12})/2$ mode for $\mathbf{q} \parallel \mathbf{a}$ and $\mathbf{q} \parallel \mathbf{b}$, seen in Fig. 2(a). We also note that while our consideration is based on the group *P6mm*, the lower symmetry of α-$RuCl_3$ may further enhance the anisotropy of the sound-attenuation coefficient along different crystallographic directions.

Turning to the longitudinal c_{11} mode, the sound velocities v_s^{La} and v_s^{Lb} from Table I for $\mathbf{q} \parallel \mathbf{a}$ and $\mathbf{q} \parallel \mathbf{b}$, respectively, are both larger than the Fermi velocity v_F, being in agreement with Ref. [62]. In this case, the pp channel dominates. These processes happen even at zero temperature, if a phonon has enough energy to excite a pair of particles [17–19]. Consequently, $\Delta\alpha(T)$ depends on temperature only above the energy scale of the phonon. In that range, thermal occupation of the fermion states will block the scattering states due to the Pauli exclusion principle. This is consistent with the downturn of c_{11} in Figs. 2(a) and 2(c). We note that asymptotically the Fermi function requires $\Delta\alpha(T) \propto T^{-1}$ for $T \gg v_F q$ [62].

Next, we comment on the relevance of the $\mathbb{Z}_2$ flux excitations for the temperature dependence of the sound attenuation. Specific-heat analysis [63,64] shows that at zero magnetic field, flux proliferation occurs in a very narrow temperature range, namely, in the vicinity of $T^\star \approx 0.01J, \ldots, 0.03J < 3\,\mathrm{K}$, which is of the order of the vison energy scale. Since $T^\star$ is clearly lower than 10 K, i.e., the temperatures for which we discuss peculiarities of the sound attenuation due to fractionalization (Fig. 2), flux excitations should play a role. Here, three comments are due. First, the fluxes do not directly scatter phonons, the spin-phonon vertex is diagonal in the flux

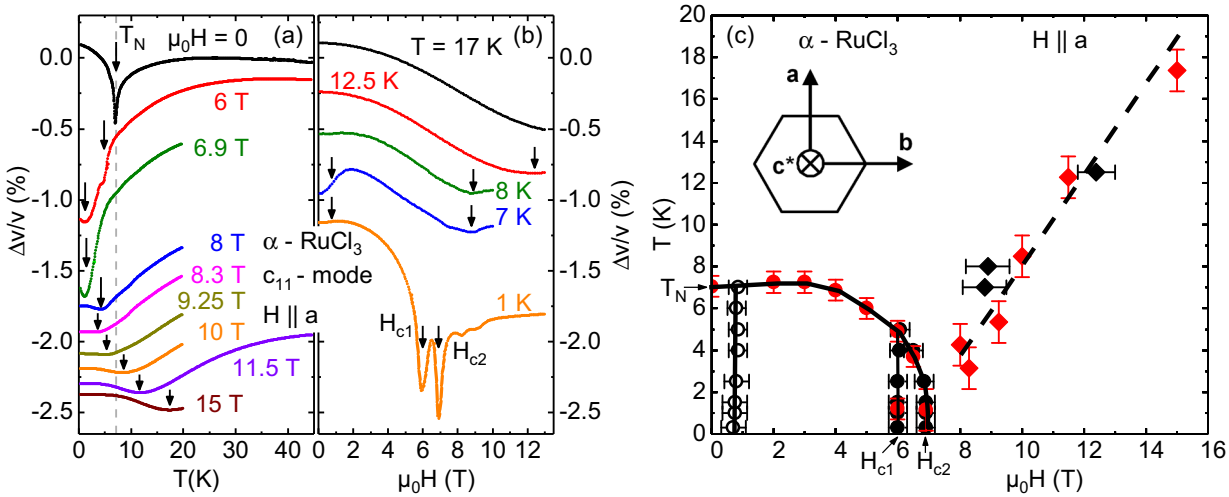

FIG. 3. (a) Temperature and (b) magnetic-field dependence of the relative sound velocity of the longitudinal acoustic mode c_{11} ($\mathbf{q} \parallel \mathbf{u} \parallel \mathbf{a}$) at selected magnetic fields ($\mathbf{H} \parallel \mathbf{a}$) and temperatures, respectively. The curves are arbitrarily shifted for clarity. The measurement frequency was $f = 22$ MHz. The vertical arrows indicate positions of the sound-velocity anomalies. T_N, H_{c1}, and H_{c2} are also shown. The gray dashed line in panel (a) corresponds to the Néel temperature T_N at zero field. (c) H-T ($\mathbf{H} \parallel \mathbf{a}$) phase diagram of α-$RuCl_3$. Characteristic temperatures (red symbols) and magnetic fields (black symbols) are extracted from the ultrasound data shown in panels (a) and (b). The lines are guides to the eye. The inset shows crystallographic directions in a honeycomb plane with the notations used in this work.

(gauge) sectors. Second, numerical treatment [17–19] clarifies, that the emergent randomness due to static $\mathbb{Z}_2$ fluxes does not obliterate the presence of a characteristic energy scale ω_c ($\omega_c = v_F q$ in the absence of $\mathbb{Z}_2$ flux excitations), such that $\Delta\alpha(T)$ scales qualitatively similar to either ph or pp scattering for phonons above or below this scale, respectively (see also Fig. 4 in Ref. [17]). While v_F of the flux-free sector is not a well-defined quantity at a finite flux density, it is reasonable to assume that $\omega_c \sim v_F q$ remains true. Hence, we believe that our arguments based on the flux-free sector are qualitatively valid even in the temperature range of interest presented in Fig. 2. Third, we stress that apart from the A_1 channel, a finite flux density will additionally reduce the anisotropy of the sound attenuation since relaxing the kinematic constraint on momenta allows for more scattering processes [19].

Finally, we note that our conclusions about the temperature dependence of the sound attenuation based on the pure Kitaev model remain valid even in the presence of small, perturbative interactions beyond the pure Kitaev limit. Recent analysis in Ref. [65] has shown that they do not destroy the T-linear dependence of the sound attenuation in the ph channel but may further reduce the anisotropy in the pp channel.

Finite-field behavior of sound attenuation. The behavior of $\Delta\alpha(T)$ in a finite magnetic field is also quite remarkable. We show corresponding data in Figs. 2(a)–2(c), mostly at 8 T, which is above the critical field $\mu_0 H_c = 6.9$ T, suppressing the zero-field magnetic zigzag order in our sample [66]. For the longitudinal mode c_{11} with $\mathbf{q} \parallel \mathbf{a}$, data are only available at 6 T, i.e., below the critical field.

In the temperature range of 10–45 K and $\mu_0 H_\mathbf{a} = 8$ T, $\Delta\alpha(T)$ of the transverse mode $(c_{11} - c_{12})/2$ for both $\mathbf{q} \parallel \mathbf{a}$ and $\mathbf{q} \parallel \mathbf{b}$ remains linear in T, consistent with the dominance of the ph processes. However, while the slope of the curve for $\mathbf{q} \parallel \mathbf{b}$ strongly increases compared with the zero-field data, it remains almost unchanged for the transverse mode with $\mathbf{q} \parallel \mathbf{a}$, such that they become similar to each other. This can be understood by the field-induced decrease of the flux-proliferation temperature $T^\star$ due to flux mobility [14,67], leading to a larger flux density at $\mu_0 H = 8$ T than at 0 T and implying less anisotropy of $\Delta\alpha(T)$ for the transverse modes at finite field.

Finite-field data for the sound attenuation of the longitudinal c_{11} mode requires more attention since it changes the character for the mode propagating along the **b** direction from pp-like behavior to ph-like behavior, but it remains pp-like for the mode propagating along the **a** direction. This is consistent with the observation that $v_s^{La} > v_s^{Lb} > v_F$ at zero field (see Table I) and with the enhanced low-T softening of the acoustic modes close to H_{c1} and H_{c2} [shown in Fig. 3(a) for the longitudinal c_{11} mode with $\mathbf{q} \parallel \mathbf{a}$]. From this, we speculate that a situation of $v_s^{Lb} < v_F$ arises at $\mu_0 H_\mathbf{a} = 8$ T and leads to the change of the character in the temperature dependence of the sound attenuation of the longitudinal c_{11} mode with $\mathbf{q} \parallel \mathbf{b}$. At 6 T and potentially at higher fields, v_s^{La} remains larger than v_F, with a sound attenuation by pp scattering. We also note that for the flux-free zero-field case, analysis of the pp channel yields $\Delta\alpha(T) \sim q^3/T$ for $T \gg q v_F$ [62]. Assuming that these estimates remain qualitatively valid at finite field and flux density and combining them with $[(q_{\|a})/(q_{\|b})]^3 \approx 1/8$ from Table I, it is conceivable that attenuation phenomena are relatively weak for the c_{11} mode with $\mathbf{q} \parallel \mathbf{a}$. For completeness we note, that the flux-free case, displays a single-fermion gap at finite magnetic field [1]. However, this does not hamper our interpretation, since thermal flux excitations readily mask this gap.

Other potential sources of the sound attenuation in α-$RuCl_3$. Let us elaborate on why we have chosen to focus on the discussion of the change in sound attenuation behavior only above 10 K. A few remarks are in order here. First, in the case of zero magnetic field, it is worth recalling that α-$RuCl_3$ undergoes a magnetic ordering phase transition at temperatures below 7 K. Thus, below 7 K, the dominant source for the sound attenuation are gapped magnons. It

is also reasonable to assume that just above this transition temperature, phonons will primarily scatter from the short-range fluctuations associated with this magnetic order. This explains the nonmonotonic behavior of sound attenuation at low temperatures observed in Figs. 2(a)–2(c). More important, however, the data show that such fluctuations, if present, have receded above 10 K and do not hamper our interpretation in terms of Majorana fermions there. Another potential reason for the low-temperature enhancement of $\Delta\alpha(T)$ could be a non-negligible amount of disorder in α-$RuCl_3$. This includes vacancies, bond-type, and stacking-type disorder [22,27]. Recent studies have shown that in the Kitaev spin liquid, disorder induces quasilocalized low-energy states, which at finite field (6 or 8 T), when dispersive fermionic modes are gapped, form in-gap low-energy bands [68–71]. These in-gap states provide an additional, predominantly pp channel for phonon scattering, bringing about an increased sound attenuation at very low temperatures. However, once the temperature increases and all these in-gap states become populated, the attenuation exhibits a decrease before starting to increase again due to the phonon-scattering processes involving dispersive Majorana modes.

Second, let us justify why we exclude some other potential origins of the observed behavior of the sound attenuation above 10 K. Lattice anharmonicity is one of them. It scales as T^3, so it can explain neither the linear T dependence observed for the transverse $(c_{11} - c_{12})/2$ mode nor the almost temperature-independent behavior of the longitudinal c_{11} mode. Moreover, the sound attenuation due to lattice anharmonicity is not field dependent.

Another potential source of the sound attenuation could be dislocations. As reported in the literature [72], dislocations might lead to a linear T dependence of $\Delta\alpha(T)$ at low temperatures but also produce a characteristic maximum in the latter at intermediate temperatures. Dislocations in α-$RuCl_3$ could result from stacking disorder of the honeycomb layers [73,74]. If dislocations would play an important role in the sound attenuation, then the acoustic modes c_{44} and c_{33} involving out of plane stress would be expected to be sensitive to them. However, we have not detected any maximum in the attenuation below the structural phase transition. See Fig. 6 of the Appendix, where we have shown the sound attenuation of the modes up to 140 K in zero field. This suggests a negligible dislocation contribution to the sound attenuation in α-$RuCl_3$.

For completeness, we clarify that sound attenuation by Fermi gases, normal as well as superconducting, can be divided into two limiting regimes [75]. Namely, (i) the clean limit, where the fermion mean-free path l_f is large compared with the phonon wavelength, i.e., $ql_f \gg 1$. And (ii) the viscous regime, in which $ql_f \ll 1$. In regime (i), sound attenuation is a pure quantum effect, i.e., phonons decay into particle-hole (particle) pairs. This is well known for clean normal metals and superconductors [76–79]. Our theoretical analysis employs this framework, yet introducing novel elements by substituting the conventional electron system with a Z_2 quantum spin liquid and replacing the electron-phonon coupling with magnetoelastic coupling. Regarding the pure spin-phonon system the fermionic clean limit is justified, since the imaginary part of the fermion self-energy is $O(T^2)$ [18]. Regarding additional extrinsic interactions, it may be of interest to clarify the relevance also of regime (ii) following, e.g., Refs. [75,80,81]. This, however, is unrelated to the work presented here. Finally, we note that sound attenuation has also been studied previously in U(1) spin liquids [15,16]. While employing fermionic spinons similarly, the latter studies also include dynamical gauge fields and fermionic lifetime effects. This differs from our Kitaev spin-liquid approach.

B. H-T phase diagram of α-$RuCl_3$

In Figs. 3(a) and 3(b), we show our results for the relative change of the sound velocity $\Delta v/v$ versus temperature and magnetic field, respectively, for the longitudinal mode c_{11} with $\mathbf{q} \parallel \mathbf{a}$ and $\mathbf{H} \parallel \mathbf{a}$. Figure 3 clearly displays anomalies, marked by black arrows, both in the temperature (a) and magnetic-field (b) dependence of $\Delta v/v$. These anomalies signal phase transitions or crossover regimes in α-$RuCl_3$. The anomaly at T_N shifts with magnetic field and an additional step-like feature together with a shallow minimum appears at about 1 K, for magnetic fields close to H_{c2}, above which the zigzag order disappears [Fig. 3(a)]. Remarkably, the elastic softening for H close to H_{c2} is at least twice as large as in zero field. Presumably, this is due to enhanced fluctuations in the quantum-critical regime. In fields $H > H_{c2}$, the velocity versus temperature exhibits a broad minimum which shifts to higher temperatures with increasing magnetic field [Fig. 3(a)]. This minimum evidences a crossover regime in this range of temperatures and magnetic fields.

The field dependence of $\Delta v/v$ in Fig. 3(b) shows two pronounced minima at $T = 1$ K (orange curve), i.e., one at $\mu_0 H_{c2} \simeq 6.9$ T and another at $\mu_0 H_{c1}$, just below the critical field, at approximately 6 T . The anomaly at H_{c2} shifts with temperature whereas H_{c1} stays constant. With H_{c2} reaching 6 T close to 5 K, both anomalies merge and for $T < T_N$ we observe a single anomaly in the field dependence. Moreover, we observe a change of curvature at small magnetic fields for temperatures below T_N. The large anomalies at 6 and 6.9 T at 1 K are related to the changes in the 3D magnetic structure between zigzag phases with different stacking orders [28,45,82] and the critical field H_{c2}, respectively. The low-field feature close to 1 T might be due to a domain rearrangement in magnetic fields [83]. Moreover, at higher temperatures, i.e., $T \geqslant 7$ K, a broad minimum appears in the sound velocity [Fig. 3(b)]. Its position correlates with the minimum observed in the temperature dependence of the sound velocity in this magnetic-field and temperature range [Fig. 3(a)].

We summarize our observations by plotting the positions of all detected anomalies on an H-T phase diagram in Fig. 3(c). Despite extensive studies [28,35,45,47,82] this is still under debate. In particular, while it is well known that magnetic fields applied along the **a** direction suppress the zigzag magnetic order in α-$RuCl_3$, leading to a spin-liquid-like state, the precise nature of this state and whether it is adiabatically connected to the high-field paramagnetic phases remains an open issue. The dashed line above 8 T is consistent with the linearly increasing spin gap detected also by other methods [47,83,84]. Remarkably, the sound-velocity minimum related to this crossover can be traced down nearly to H_{c2}.

IV. CONCLUSION

We present the temperature and in-plane magnetic-field dependence of the relative velocity and attenuation of longitudinal and transverse sound waves in α-$RuCl_3$. Strong spin-lattice coupling allows our ultrasound measurements to uncover remarkably rich information about the magnetic ground state and excitations of this material. We argue that the peculiar behavior of the sound attenuation in α-$RuCl_3$ over a wide range of temperatures can be understood as a fingerprint of the fractionalized excitations of a Kitaev magnet with comparable Fermi and sound velocities: transverse sound modes with smaller velocities scatter off from particle-hole excitations, inducing a characteristic T-linear damping, while longitudinal modes with higher velocities tap into the fermionic particle-particle continuum at zero field. The $\mathbb{Z}_2$ flux excitations are relevant to lift part of the symmetry-required anisotropies of the attenuation, as well as to explain its high-field behavior. Our data suggest the striking scenario of a field-driven tuning of one of the longitudinal sound velocities through the Fermi velocity. Likely, these findings survive inclusion of further exchange interactions in the QSL phase [65]. Regarding the sound velocity, we identify a large set of transitions in temperature and in-plane magnetic-field dependencies, and draw an H-T phase diagram, consistent with previous work by other methods.

ACKNOWLEDGMENTS

We thank Markus König at the Max Planck Institute for Chemical Physics of Solids in Dresden for the technical support in the focused-ion-beam assisted polishing process. We acknowledge support of the HLD at HZDR, member of the European Magnetic Field Laboratory (EMFL). The work of S.Z., W.B., A.H., and J.W. has been supported in part by the DFG through SFB 1143 (project-id 247310070). The work of A.H. and J.W. has been supported in part by the DFG through excellence cluster *ct.qmat* (EXC 2147, project-id 39085490). W.B. acknowledges kind hospitality of the PSM, Dresden. The work of N.B.P. was supported by the U.S. Department of Energy, Office of Science, Basic Energy Sciences under Award No. DE-SC0018056. N.B.P. also acknowledges the hospitality and partial support of the Technical University of Munich - Institute for Advanced Study. M.Y. was supported by a grant from the Simons Foundation (216179, LB) and by the National Science Foundation under Grant No. NSF PHY-1748958. The work of K.Y.C. at SKKU is supported by the National Research Foundation (NRF) of Korea (Grant No. 2020R1A5A1016518). The work of V.T. was supported by the DFG through Transregional Research Collaboration TRR 80 (Augsburg, Munich, and Stuttgart) as well as by the project ANCD 20.80009.5007.19 (Moldova). Finally, M.Y., W.B., and N.B.P. acknowledge the support by the National Science Foundation under Grant No. NSF PHY-1748958 and the hospitality of KITP, UC Santa Barbara, where part of this work was finalized.

APPENDIX A: ULTRASOUND PULSED-ECHO TECHNIQUE

In this work, we utilize the ultrasound pulse-echo phase-sensitive detection technique [52] that is suitable for experiments at low temperatures, high magnetic fields, and under hydrostatic pressures. This technique is based on the homodyne method and allows the simultaneous measurement of the sound velocity, $\Delta v/v$, and sound attenuation, $\Delta\alpha$. The measurement setup used in this work is schematically shown in Fig. 4.

First, a signal generator produces radio-frequency signal (cw) of the form $B = B_0\cos(\omega t)$, with angular frequency $\omega = 2\pi f$, in the frequency range $f = 10$–500 MHz. The signal is then divided with a voltage divider to a reference channel and signal channel. A quadrature hybrid in the reference channel provides two reference signals with equal frequency but with 0° and 90° phase shift, respectively. The signal channel contains a switch driven by the pulse generator to form the

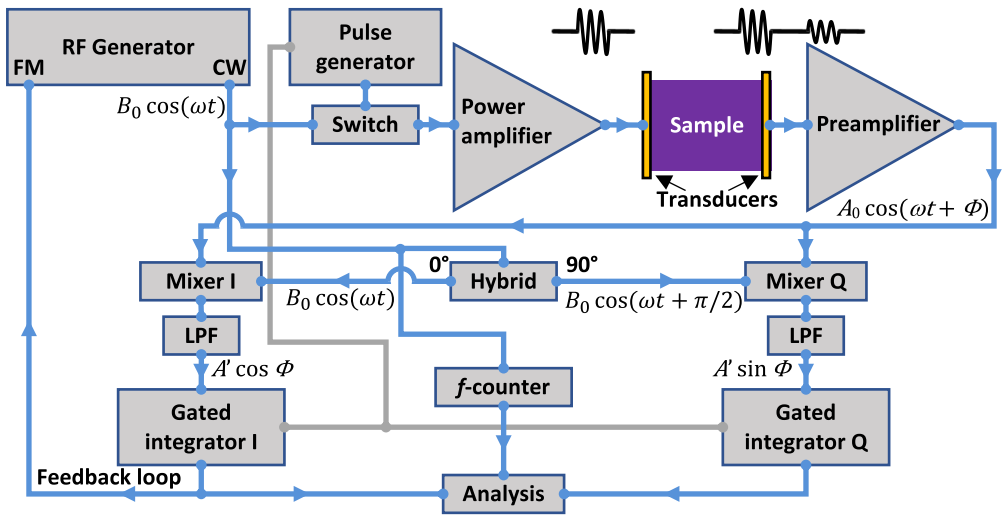

FIG. 4. Schematic illustration of the ultrasound setup based on the homodyne method for the simultaneous measurement of the sound velocity and sound attenuation.

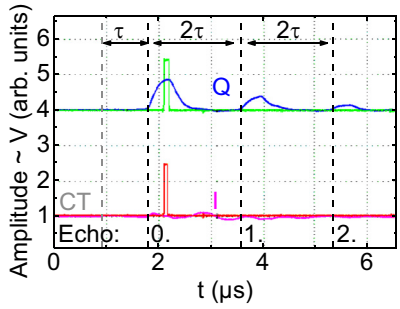

FIG. 5. Echo train for the transverse $(c_{11} - c_{12})/2$ mode ($q \parallel a$) in α-$RuCl_3$ at 200 K. The Q (blue) and I signal (purple) are shown versus time together with the ranges averaged by means of gated integrator (green and red gates). Vertical, dashed lines show the onset of crosstalk (CT, gray) and onset of echoes (black) $n = 0$ (first transmitting signal), 1, and 2. In the present work all measurements were performed at zero echo. Note, that for different echoes, n, the effective sample length should be used $L' = L(2n + 1)$. $\tau = L/v$ is the time required by the sound to travel through the sample length L with the velocity v. Hence, the absolute sound velocity can be obtained.

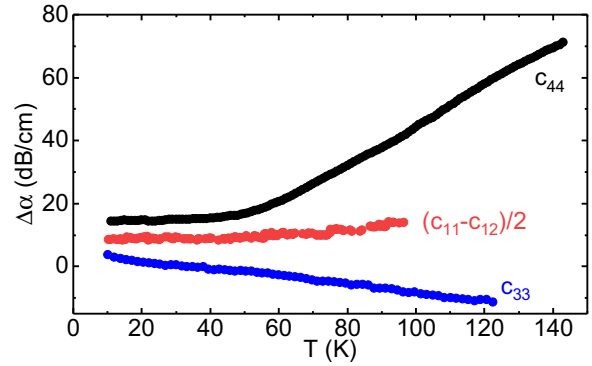

FIG. 6. Ultrasound-attenuation change for the elastic modes c_{44} (**k** ∥ **b**, **u** ∥ **c**), $(c_{11} - c_{12})/2$ (**k** ∥ **b**, **u** ∥ **a**), and c_{33} (**k** ∥ **u** ∥ **c**) versus temperature in α-$RuCl_3$ up to 140 K in zero field.

radio-frequency pulses with a typical pulse duration of 100 to 500 ns and repetition rate of a few kHz. After the amplification (up to a few volts amplitude), these pulses excite a piezoelectric ultrasonic transducer bonded to the sample. The second transducer detects the ultrasound signal on the opposite side of the sample and transforms it back into a high-frequency voltage signal.

In the sample, the signal undergoes a phase shift Φ and a change of the amplitude depending on external parameters such as magnetic field or temperature. The signal takes the form $A = A_0 \cos(\omega t + \Phi)$. During the signal detection, the signal is amplified by a broadband low-noise preamplifier and mixed with both reference signals. A low-pass filter (LPF) removes double-frequency signal components, extracting the amplitude and phase information in-phase (0°) and quadrature (90°) channels, denoted as I and Q, respectively [52,85]:

$$\begin{aligned} I &= (1/2)A_0B_0\cos\Phi, \\ Q &= (1/2)A_0B_0\sin\Phi. \end{aligned} \tag{A1}$$

One can consider I and Q as Cartesian coordinates related to the signal with the amplitude $A' = (I^2 + Q^2)^{1/2}$ and phase Φ represented in polar coordinates.

The measured sound-velocity change is [52]

$$\Delta v/v = \Delta f/f - \Delta\Phi/\Phi + \Delta L/L. \tag{A2}$$

The sample-length change [last term in Eq. (A2)] is typically very small and can be neglected. In the pulsed-magnetic-field experiments the frequency is fixed [first term on the right side of Eq. (A2) is zero] and the sound-velocity change is proportional to the phase change. At constant frequency $\Delta f = 0$, the phase is determined from I and Q as $\Phi = \arctan(Q/I)$. Instead, in static-field experiments the phase Φ is typically locked ($\Delta\Phi = 0$) by a feedback loop based on the frequency modulation (FM) by a DC signal regulating I to zero by adjusting the ultrasonic frequency. The sound-velocity change is proportional to the frequency change in this case, increasing the measurement accuracy to typically 10^{-6}. The signals in the channels I and Q are averaged by means of gated integrators (boxcar averagers) at the gate position. Typically, an average value of 1000 repetitions is collected. The information from both channels and the measured frequency together with temperature and magnetic field are saved for further analysis.

The sound attenuation change $\Delta\alpha(T, H)$ is calculated with respect to the attenuation initial value $\alpha(T_0, H_0)$ at a chosen temperature T_0 and magnetic field H_0 (e.g., in zero-field at lowest temperature) as $\Delta\alpha(T, H) = \alpha(T, H) - \alpha(T_0, H_0) = 20(\log_{10}[B_0'/A'(T, H)] - \log_{10}[B_0'/A'(T_0, H_0)])/L = -20\log_{10}[A'(T, H)/A'(T_0, H_0)]/L$ [53]. Here, B_0' is a sound-excitation amplitude and A' is the amplitude of the detected sound signal. Note, for each new sample installation the direct comparison of the absolute values of ultrasonic attenuation α is not possible due to unknown losses in the transducers and in the bond, diffraction effects, and phonon focusing [52]. This results in different initial values of the sound excitation amplitude B_0'. Only the relative change, $\Delta\alpha(T, H)$, can be compared in this case. A characteristic output of a measured signal in the oscilloscope is shown in Fig. 5. The oscilloscope channels show signal Q (blue), signal I (purple) and the clocked gates of the boxcar averager (green and red, respectively). During a measurement, the two gates are set to the same temporal position and span.

APPENDIX B: ULTRASOUND ATTENUATION BEYOND THE ORDERED STATE

Figure 6 shows the ultrasound-attenuation change versus temperature for the acoustic modes c_{44}, $(c_{11} - c_{12})/2$, and c_{33} up to 140 K.

[1] A. Kitaev, Anyons in an exactly solved model and beyond, Ann. Phys. (NY) **321**, 2 (2006).

[2] G. Baskaran, S. Mandal, and R. Shankar, Exact results for spin dynamics and fractionalization in the Kitaev model, Phys. Rev. Lett. **98**, 247201 (2007).

[3] J. Knolle, D. L. Kovrizhin, J. T. Chalker, and R. Moessner, Dynamics of a two-dimensional quantum spin liquid: Signatures of emergent Majorana fermions and fluxes, Phys. Rev. Lett. **112**, 207203 (2014).

[4] J. Knolle, D. L. Kovrizhin, J. T. Chalker, and R. Moessner, Dynamics of fractionalization in quantum spin liquids, Phys. Rev. B **92**, 115127 (2015).

[5] J. Knolle, G.-W. Chern, D. L. Kovrizhin, R. Moessner, and N. B. Perkins, Raman scattering signatures of kitaev spin liquids in A_2IrO_3 iridates with $A =$ Na or Li, Phys. Rev. Lett. **113**, 187201 (2014).

[6] J. Nasu, M. Udagawa, and Y. Motome, Vaporization of Kitaev spin liquids, Phys. Rev. Lett. **113**, 197205 (2014).

[7] J. Nasu, J. Knolle, D. L. Kovrizhin, Y. Motome, and R. Moessner, Fermionic response from fractionalization in an insulating two-dimensional magnet, Nat. Phys. **12**, 912 (2016).

[8] G. B. Halász, N. B. Perkins, and J. van den Brink, Resonant inelastic x-ray scattering response of the Kitaev honeycomb model, Phys. Rev. Lett. **117**, 127203 (2016).

[9] G. B. Halász, S. Kourtis, J. Knolle, and N. B. Perkins, Observing spin fractionalization in the Kitaev spin liquid via temperature evolution of indirect resonant inelastic x-ray scattering, Phys. Rev. B **99**, 184417 (2019).

[10] I. Rousochatzakis, S. Kourtis, J. Knolle, R. Moessner, and N. B. Perkins, Quantum spin liquid at finite temperature: Proximate dynamics and persistent typicality, Phys. Rev. B **100**, 045117 (2019).

[11] M. Udagawa, S. Takayoshi, and T. Oka, Scanning tunneling microscopy as a single Majorana detector of Kitaev's chiral spin liquid, Phys. Rev. Lett. **126**, 127201 (2021).

[12] M. Hermanns, I. Kimchi, and J. Knolle, Physics of the Kitaev model: Fractionalization, dynamic correlations, and material connections, Annu. Rev. Condens. Matter Phys. **9**, 17 (2018).

[13] Y. Motome and J. Nasu, Hunting Majorana fermions in Kitaev magnets, J. Phys. Soc. Jpn. **89**, 012002 (2020).

[14] S. Trebst and C. Hickey, Kitaev materials, Phys. Rep. **950**, 1 (2022).

[15] Y. Zhou and P. A. Lee, Spinon phonon interaction and ultrasonic attenuation in quantum spin liquids, Phys. Rev. Lett. **106**, 056402 (2011).

[16] M. Serbyn and P. A. Lee, Spinon-phonon interaction in algebraic spin liquids, Phys. Rev. B **87**, 174424 (2013).

[17] A. Metavitsiadis and W. Brenig, Phonon renormalization in the Kitaev quantum spin liquid, Phys. Rev. B **101**, 035103 (2020).

[18] M. Ye, R. M. Fernandes, and N. B. Perkins, Phonon dynamics in the Kitaev spin liquid, Phys. Rev. Res. **2**, 033180 (2020).

[19] K. Feng, M. Ye, and N. B. Perkins, Temperature evolution of the phonon dynamics in the Kitaev spin liquid, Phys. Rev. B **103**, 214416 (2021).

[20] A. Metavitsiadis, W. Natori, J. Knolle, and W. Brenig, Optical phonons coupled to a Kitaev spin liquid, Phys. Rev. B **105**, 165151 (2022).

[21] K. Feng, S. Swarup, and N. B. Perkins, Footprints of Kitaev spin liquid in the Fano lineshape of Raman-active optical phonons, Phys. Rev. B **105**, L121108 (2022).

[22] K. W. Plumb, J. P. Clancy, L. J. Sandilands, V. V. Shankar, Y. F. Hu, K. S. Burch, H.-Y. Kee, and Y.-J. Kim, α-$RuCl_3$: A spin-orbit assisted Mott insulator on a honeycomb lattice, Phys. Rev. B **90**, 041112(R) (2014).

[23] A. Banerjee, J. Yan, J. Knolle, C. A. Bridges, M. B. Stone, M. D. Lumsden, D. G. Mandrus, D. A. Tennant, R. Moessner, and S. E. Nagler, Neutron scattering in the proximate quantum spin liquid α-$RuCl_3$, Science **356**, 1055 (2017).

[24] S.-H. Do, S.-Y. Park, J. Yoshitake, J. Nasu, Y. Motome, Y. Kwon, D. T. Adroja, D. J. Voneshen, K. Kim, T.-H. Jang, J.-H. Park, K.-Y. Choi, and S. Ji, Majorana fermions in the Kitaev quantum spin system α-$RuCl_3$, Nat. Phys. **13**, 1079 (2017).

[25] N. Janša, A. Zorko, M. Gomilšek, M. Pregelj, K. W. Krämer, D. Biner, A. Biffin, C. Rüegg, and M. Klanjšek, Observation of two types of fractional excitation in the Kitaev honeycomb magnet, Nat. Phys. **14**, 786 (2018).

[26] H. Takagi, T. Takayama, G. Jackeli, G. Khaliullin, and S. E. Nagler, Concept and realization of Kitaev quantum spin liquids, Nat. Rev. Phys. **1**, 264 (2019).

[27] J. A. Sears, M. Songvilay, K. W. Plumb, J. P. Clancy, Y. Qiu, Y. Zhao, D. Parshall, and Y.-J. Kim, Magnetic order in α-$RuCl_3$: A honeycomb-lattice quantum magnet with strong spin-orbit coupling, Phys. Rev. B **91**, 144420 (2015).

[28] C. Balz, L. Janssen, P. Lampen-Kelley, A. Banerjee, Y. H. Liu, J.-Q. Yan, D. G. Mandrus, M. Vojta, and S. E. Nagler, Field-induced intermediate ordered phase and anisotropic interlayer interactions in α-$RuCl_3$, Phys. Rev. B **103**, 174417 (2021).

[29] H. Suzuki, H. Liu, J. Bertinshaw, K. Ueda, H. Kim, S. Laha, D. Weber, Z. Yang, L. Wang, H. Takahashi, K. Fürsich, M. Minola, B. V. Lotsch, B. J. Kim, H. Yavaş, M. Daghofer, J. Chaloupka, G. Khaliullin, H. Gretarsson, and B. Keimer, Proximate ferromagnetic state in the Kitaev model material α-$RuCl_3$, Nat. Commun. **12**, 4512 (2021).

[30] J. Wagner, A. Sahasrabudhe, R. B. Versteeg, L. Wysocki, Z. Wang, V. Tsurkan, A. Loidl, D. I. Khomskii, H. Hedayat, and P. H. M. van Loosdrecht, Magneto-optical study of metamagnetic transitions in the antiferromagnetic phase of α-$RuCl_3$, npj Quantum Mater. **7**, 28 (2022).

[31] S. Bachus, D. A. S. Kaib, Y. Tokiwa, A. Jesche, V. Tsurkan, A. Loidl, S. M. Winter, A. A. Tsirlin, R. Valentí, and P. Gegenwart, Thermodynamic perspective on field-induced behavior of α-$RuCl_3$, Phys. Rev. Lett. **125**, 097203 (2020).

[32] H. Li, H.-K. Zhang, J. Wang, H.-Q. Wu, Y. Gao, D.-W. Qu, Z.-X. Liu, S.-S. Gong, and W. Li, Identification of magnetic interactions and high-field quantum spin liquid in α-$RuCl_3$, Nat. Commun. **12**, 4007 (2021).

[33] P. Laurell and S. Okamoto, Dynamical and thermal magnetic properties of the Kitaev spin liquid candidate α-$RuCl_3$, npj Quantum Mater. **5**, 2 (2020).

[34] K. A. Modic, R. D. McDonald, J. P. C. Ruff, M. D. Bachmann, Y. Lai, J. C. Palmstrom, D. Graf, M. K. Chan, F. F. Balakirev, J. B. Betts, G. S. Boebinger, M. Schmidt, M. J. Lawler, D. A. Sokolov, P. J. W. Moll, B. J. Ramshaw, and A. Shekhter, Scale-invariant magnetic anisotropy in α-$RuCl_3$ at high magnetic fields, Nat. Phys. **17**, 240 (2021).

[35] S.-H. Baek, S.-H. Do, K.-Y. Choi, Y. S. Kwon, A. U. B. Wolter, S. Nishimoto, J. van den Brink, and B. Büchner, Evidence for a field-induced quantum spin liquid in α-$RuCl_3$, Phys. Rev. Lett. **119**, 037201 (2017).

[36] A. U. B. Wolter and C. Hess, Spin liquid evidence at the edge and in bulk, Nat. Phys. **18**, 378 (2022).

[37] Y. Kasahara, T. Ohnishi, Y. Mizukami, O. Tanaka, S. Ma, K. Sugii, N. Kurita, H. Tanaka, J. Nasu, Y. Motome, T. Shibauchi, and Y. Matsuda, Majorana quantization and half-integer thermal quantum Hall effect in a Kitaev spin liquid, Nature (London) **559**, 227 (2018).

[38] O. Tanaka, Y. Mizukami, R. Harasawa, K. Hashimoto, K. Hwang, N. Kurita, H. Tanaka, S. Fujimoto, Y. Matsuda, E.-G. Moon, and T. Shibauchi, Thermodynamic evidence for a field-angle-dependent Majorana gap in a Kitaev spin liquid, Nat. Phys. **18**, 429 (2022).

[39] T. Yokoi, S. Ma, Y. Kasahara, S. Kasahara, T. Shibauchi, N. Kurita, H. Tanaka, J. Nasu, Y. Motome, C. Hickey, S. Trebst, and Y. Matsuda, Half-integer quantized anomalous thermal Hall effect in the Kitaev material candidate α-$RuCl_3$, Science **373**, 568 (2021).

[40] S. Bachus, D. A. S. Kaib, A. Jesche, V. Tsurkan, A. Loidl, S. M. Winter, A. A. Tsirlin, R. Valentí, and P. Gegenwart, Angle-dependent thermodynamics of α-$RuCl_3$, Phys. Rev. B **103**, 054440 (2021).

[41] M. Ye, G. B. Halász, L. Savary, and L. Balents, Quantization of the thermal Hall conductivity at small Hall angles, Phys. Rev. Lett. **121**, 147201 (2018).

[42] Y. Vinkler-Aviv and A. Rosch, Approximately quantized thermal Hall effect of chiral liquids coupled to phonons, Phys. Rev. X **8**, 031032 (2018).

[43] V. Kocsis, D. A. S. Kaib, K. Riedl, S. Gass, P. Lampen-Kelley, D. G. Mandrus, S. E. Nagler, N. Pérez, K. Nielsch, B. Büchner, A. U. B. Wolter, and R. Valentí, Magnetoelastic coupling anisotropy in the Kitaev material α-$RuCl_3$, Phys. Rev. B **105**, 094410 (2022).

[44] D. A. S. Kaib, S. Biswas, K. Riedl, S. M. Winter, and R. Valentí, Magnetoelastic coupling and effects of uniaxial strain in α-$RuCl_3$ from first principles, Phys. Rev. B **103**, L140402 (2021).

[45] R. Schönemann, S. Imajo, F. Weickert, J. Yan, D. G. Mandrus, Y. Takano, E. L. Brosha, P. F. S. Rosa, S. E. Nagler, K. Kindo, and M. Jaime, Thermal and magnetoelastic properties of α-$RuCl_3$ in the field-induced low-temperature states, Phys. Rev. B **102**, 214432 (2020).

[46] S. Mu, K. D. Dixit, X. Wang, D. L. Abernathy, H. Cao, S. E. Nagler, J. Yan, P. Lampen-Kelley, D. Mandrus, C. A. Polanco, L. Liang, G. B. Halász, Y. Cheng, A. Banerjee, and T. Berlijn, Role of the third dimension in searching for Majorana fermions in α-$RuCl_3$ via phonons, Phys. Rev. Res. **4**, 013067 (2022).

[47] R. Hentrich, A. U. B. Wolter, X. Zotos, W. Brenig, D. Nowak, A. Isaeva, T. Doert, A. Banerjee, P. Lampen-Kelley, D. G. Mandrus, S. E. Nagler, J. Sears, Y.-J. Kim, B. Büchner, and C. Hess, Unusual phonon heat transport in α-$RuCl_3$: Strong spin-phonon scattering and field-induced spin gap, Phys. Rev. Lett. **120**, 117204 (2018).

[48] H. Li, T. T. Zhang, A. Said, G. Fabbris, D. G. Mazzone, J. Q. Yan, D. Mandrus, G. B. Halász, S. Okamoto, S. Murakami, M. P. M. Dean, H. N. Lee, and H. Miao, Giant phonon anomalies in the proximate Kitaev quantum spin liquid α-$RuCl_3$, Nat. Commun. **12**, 3513 (2021).

[49] S. Reschke, V. Tsurkan, S.-H. Do, K.-Y. Choi, P. Lunkenheimer, Z. Wang, and A. Loidl, Terahertz excitations in α-$RuCl_3$: Majorana fermions and rigid-plane shear and compression modes, Phys. Rev. B **100**, 100403(R) (2019).

[50] J. A. N. Bruin, R. R. Claus, Y. Matsumoto, N. Kurita, H. Tanaka, and H. Takagi, Robustness of the thermal Hall effect close to half-quantization in α-$RuCl_3$, Nat. Phys. **18**, 401 (2022).

[51] M. Yamashita, J. Gouchi, Y. Uwatoko, N. Kurita, and H. Tanaka, Sample dependence of half-integer quantized thermal Hall effect in the Kitaev spin-liquid candidate α-$RuCl_3$, Phys. Rev. B **102**, 220404(R) (2020).

[52] B. Lüthi, *Physical Acoustics in the Solid State* (Springer, Berlin, Heidelberg, New York, 2005).

[53] R. Truell, C. Elbaum, and B. B. Chick, *Ultrasonic Methods in Solid State Physics* (Academic Press, New York, London, 1969).

[54] S. Reschke, F. Mayr, S. Widmann, H.-A. K. von Nidda, V. Tsurkan, M. V. Eremin, S.-H. Do, K.-Y. Choi, Z. Wang, and A. Loidl, Sub-gap optical response in the Kitaev spin-liquid candidate α-$RuCl_3$, J. Phys.: Condens. Matter **30**, 475604 (2018).

[55] H. B. Cao, A. Banerjee, J.-Q. Yan, C. A. Bridges, M. D. Lumsden, D. G. Mandrus, D. A. Tennant, B. C. Chakoumakos, and S. E. Nagler, Low-temperature crystal and magnetic structure of α-$RuCl_3$, Phys. Rev. B **93**, 134423 (2016).

[56] B. W. Lebert, S. Kim, D. A. Prishchenko, A. A. Tsirlin, A. H. Said, A. Alatas, and Y.-J. Kim, Acoustic phonon dispersion of α-$RuCl_3$, Phys. Rev. B **106**, L041102 (2022).

[57] S. Zherlitsyn, S. S. Yasin, J. Wosnitza, A. Zvyagin, A. Andreev, and V. Tsurkan, Spin-lattice effects in selected antiferromagnetic materials, Low Temp. Phys. **40**, 123 (2014).

[58] Y. Kubota, H. Tanaka, T. Ono, Y. Narumi, and K. Kindo, Successive magnetic phase transitions in α-$RuCl_3$: XY-like frustrated magnet on the honeycomb lattice, Phys. Rev. B **91**, 094422 (2015).

[59] B. Lüthi, T. J. Moran, and R. J. Pollina, Sound propagation near magnetic phase transitions, J. Phys. Chem. Solids **31**, 1741 (1970).

[60] A. Glamazda, P. Lemmens, S.-H. Do, Y. S. Kwon, and K.-Y. Choi, Relation between Kitaev magnetism and structure in α-$RuCl_3$, Phys. Rev. B **95**, 174429 (2017).

[61] S.-Y. Park, S.-H. Do, K.-Y. Choi, D. Jang, T.-H. Jang, J. Schefer, C.-M. Wu, J. S. Gardner, J. M. S. Park, J.-H. Park, and S. Ji, Emergence of the isotropic Kitaev honeycomb lattice α-$RuCl_3$ and its magnetic properties, J. Phys.: Condens. Matter **36**, 215803 (2024).

[62] H. Li, A. Said, J. Q. Yan, D. M. Mandrus, H. N. Lee, S. Okamoto, G. B. Halász, and H. Miao, Divergence of Majorana-phonon scattering in Kitaev quantum spin liquid, arXiv:2112.02015.

[63] J. Nasu, M. Udagawa, and Y. Motome, Thermal fractionalization of quantum spins in a Kitaev model: Temperature-linear specific heat and coherent transport of Majorana fermions, Phys. Rev. B **92**, 115122 (2015).

[64] A. Metavitsiadis, A. Pidatella, and W. Brenig, Thermal transport in a two-dimensional $\mathbb{Z}_2$ spin liquid, Phys. Rev. B **96**, 205121 (2017).

[65] S. Singh, P. P. Stavropoulos, and N. B. Perkins, Phonon dynamics in the generalized Kitaev spin liquid, Phys. Rev. B **107**, 214428 (2023).

[66] Z. Wang, S. Reschke, D. Hüvonen, S.-H. Do, K.-Y. Choi, M. Gensch, U. Nagel, T. Room, and A. Loidl, Magnetic excitations

and continuum of a possibly field-induced quantum spin liquid in α-$RuCl_3$, Phys. Rev. Lett. **119**, 227202 (2017).

[67] A. Metavitsiadis and W. Brenig, Flux mobility delocalization in the Kitaev spin ladder, Phys. Rev. B **103**, 195102 (2021).

[68] J. Knolle, R. Moessner, and N. B. Perkins, Bond-disordered spin liquid and the honeycomb iridate $H_3LiIr_2O_6$: Abundant low-energy density of states from random Majorana hopping, Phys. Rev. Lett. **122**, 047202 (2019).

[69] W.-H. Kao, J. Knolle, G. B. Halász, R. Moessner, and N. B. Perkins, Vacancy-induced low-energy density of states in the Kitaev spin liquid, Phys. Rev. X **11**, 011034 (2021).

[70] W.-H. Kao and N. B. Perkins, Disorder upon disorder: Localization effects in the Kitaev spin liquid, Ann. Phys. (NY) **435**, 168506 (2021).

[71] V. Dantas and E. C. Andrade, Disorder, low-energy excitations, and topology in the Kitaev spin liquid, Phys. Rev. Lett. **129**, 037204 (2022).

[72] W. A. Fate, Thermal damping of dislocations in copper and lead, J. Appl. Phys. **43**, 835 (1972).

[73] X. Mi, X. Wang, H. Gui, M. Pi, T. Zheng, K. Yang, Y. Gan, P. Wang, A. Li, A. Wang, L. Zhang, Y. Su, Y. Chai, and M. He, Stacking faults in α-$RuCl_3$ revealed by local electric polarization, Phys. Rev. B **103**, 174413 (2021).

[74] H. Zhang, M. A. McGuire, A. F. May, J. Chao, Q. Zheng, M. Chi, B. C. Sales, D. G. Mandrus, S. E. Nagler, H. Miao, F. Ye, and J. Yan, Stacking disorder and thermal transport properties of α-$RuCl_3$, Phys. Rev. Mater. **8**, 014402 (2024).

[75] F. S. Khan and P. B. Allen, Sound attenuation by electrons in metals, Phys. Rev. B **35**, 1002 (1987).

[76] P. B. Allen, Neutron spectroscopy of superconductors, Phys. Rev. B **6**, 2577 (1972).

[77] P. B. Allen, Acoustic phonon damping in cubic metals, Solid State Commun. **13**, 311 (1973).

[78] S. M. Shapiro, G. Shirane, and J. D. Axe, Measurements of the electron-phonon interaction in nb by inelastic neutron scattering, Phys. Rev. B **12**, 4899 (1975).

[79] K. Hong and J. Carbotte, Finite frequency ultrasonic attenuation in strong coupling superconductors, Solid State Commun. **22**, 299 (1977).

[80] D. Belitz, Electron-phonon interaction, ultrasonic attenuation, and Eliashberg function $\alpha^2 F(\omega)$ in impure metals, Phys. Rev. B **36**, 2513 (1987).

[81] M. Y. Reizer, Temperature dependence of sound attenuation in impure metals, Phys. Rev. B **40**, 7461 (1989).

[82] C. Balz, P. Lampen-Kelley, A. Banerjee, J. Yan, Z. Lu, X. Hu, S. M. Yadav, Y. Takano, Y. Liu, D. A. Tennant, M. D. Lumsden, D. Mandrus, and S. E. Nagler, Finite field regime for a quantum spin liquid in α-$RuCl_3$, Phys. Rev. B **100**, 060405(R) (2019).

[83] J. A. Sears, Y. Zhao, Z. Xu, J. W. Lynn, and Y.-J. Kim, Phase diagram of α-$RuCl_3$ in an in-plane magnetic field, Phys. Rev. B **95**, 180411(R) (2017).

[84] A. U. B. Wolter, L. T. Corredor, L. Janssen, K. Nenkov, S. Schönecker, S.-H. Do, K.-Y. Choi, R. Albrecht, J. Hunger, T. Doert, M. Vojta, and B. Büchner, Field-induced quantum criticality in the Kitaev system α-$RuCl_3$, Phys. Rev. B **96**, 041405(R) (2017).

[85] B. Wolf, B. Lüthi, S. Schmidt, H. Schwenk, M. Sieling, S. Zherlitsyn, and I. Kouroudis, New experimental techniques for pulsed magnetic fields - ESR and ultrasonics, Phys. B (Amsterdam, Neth.) **294-295**, 612 (2001).